# GUIDANCE, NAVIGATION AND CONTROL ADVANCES IN ELECTROSTATIC ATTITUDE CONTROL ON PASSIVE GEO OBJECTS

**Trevor Bennett*** **and Hanspeter Schaub†**

Electrostatic detumble and electrostatic actuation technologies are currently considered for challenging space missions including satellite servicing, satellite tugging, and active debris removal. These touchless electrostatic actuation applications capitalize on the servicing craft's relative position to improve performance, estimate charging characteristics, or deliver specific orbit element changes. Therefore, modeling and control of the relative position is of critical importance. This paper presents an overview of recent formation flying developments in electrostatic actuation with additional developments in estimation of relative position and charging properties. The benefits of electrostatic attitude control while doing formation flying are analyzed from guidance, navigation, and control perspectives. Numerical simulations are presented that demonstrate the advantages of a formation flying perspective.

## INTRODUCTION

The Geostationary orbit (GEO) is one of the most valuable Earth orbiting regions requiring operators to maintain tight orbital slots and adhere to end-of-life practices to protect assets insured over 13 Billion US dollars.[1] Despite these practices, some uncontrolled objects still threaten continued operation in GEO motivating servicing or debris removal strategies.[2] Touchless methods are of greatest interest for some of the GEO targets because some candidate targets tumble at rates up to 10 degrees per second far exceeding the capability of mechanical interfaces.[3–5] There are a variety of proposed methods for soft docking or flexible interface on a target object; most notably harpoons and nets.[6–8] Most promising are touchless methods of on-orbit actuation with an active service vehicle. Eddy-current detumble reduces the rotation of the target through the interaction between eddy-currents generated in the target object and the Earth's magnetic field.[9–11] The Ion-Shepherd method utilizes the thrust impingement of the servicer craft on the target to reduce rotation rates.[12–14] The touches application considered in this study is electrostatic actuation of the target craft.

Electrostatic actuation encompasses a diverse range of on-orbit capability from target re/deorbiting, electrostatic structure inflation, active and assisted debris detumbling, and the opportunity for non-Keplerian relative orbits. Electrostatic actuation of spacecraft has been explored as early as the 1960s developing both the understanding of charging dynamics and on-orbit uses such as structure inflation.[15,16] Continued work explores the effect of Lorentz force on a single Earth-orbiting satellite.[17,18] Several authors have gone further to explore the use of electrostatics for formation flying of multiple craft in non-Kelperian orbits.[19–22] Earlier work explores charged formation flying with Coulomb debris tug trajectories[23,24] and use Coulomb and Lorentz forces.[25–27]

*Graduate Research Assistant, Aerospace Engineering Sciences, University of Colorado Boulder.

†Alfred T. and Betty E. Look Professor of Engineering, Associate Chair of Graduate Affairs, Department of Aerospace Engineering Sciences, University of Colorado, 431 UCB, Colorado Center for Astrodynamics Research, Boulder, CO 80309-0431

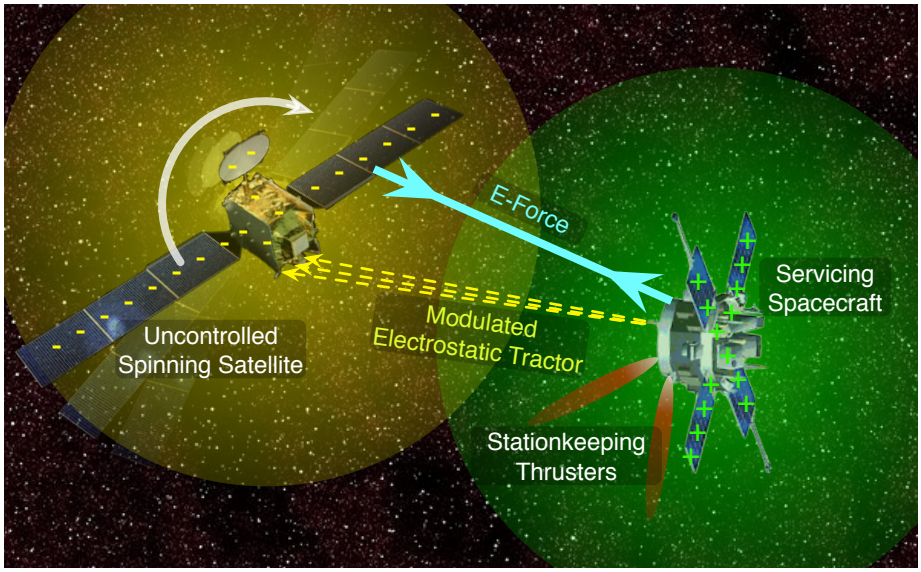


**Figure 1. Electrostatic actuation technology enabling diverse service mission profiles.**

In addition, electrostatic actuation with a passive object is being considered for large GEO debris mitigation.[24,28–30] Electrostatic detumble builds upon these electrostatic actuation developments to provide an active detumble capability. Specifically, Reference 15 shows that the Geosynchronous Orbit environment is a prime candidate region where space plasma conditions enable electrostatic interaction across 10's to 100's of meters requiring only Watt-levels of power. Reference 31 first introduced how electrostatic charging can be controlled to apply torques on a spinning debris object without requiring physical contact as shown in Figure 1.

Formation flying is a critical component of electrostatic actuation because the servicer craft operates within tens of meters of the target. At such ranges, formation flying formulations present more insightful prediction and control. Reference 32 explores how a lead-follower formation removes additional angular momentum through systematic change in the relative position. It is shown that the lead-follower relative orbit completely detumbles the cylinder over the course of 11 days where the fixed servicer position is in general only capable of partial detumble. Additional developments show that an optimal servicer relative position can be computed for electrostatic detumble of a cylindrical target craft.[33]

The current challenge is to distill the detumble-improving formation flying influences and capitalize on relative motion in the guidance, navigation, and control of the servicer spacecraft. The Linearized Relative Orbit Element (LROE) relative position description is proposed for all formation flying analysis.[34] These elements have been estimated from pose measurements.[35] Presented here are additional estimation formulations that capture electrostatic potential of the target craft in addition to the relative position. The combination of the LROE kinematic description, estimation of the relative position and spacecraft charging, and the control of the servicer position are discussed in the following sections. The insight of formation flying on two representative target craft is demonstrated through numerical simulations.

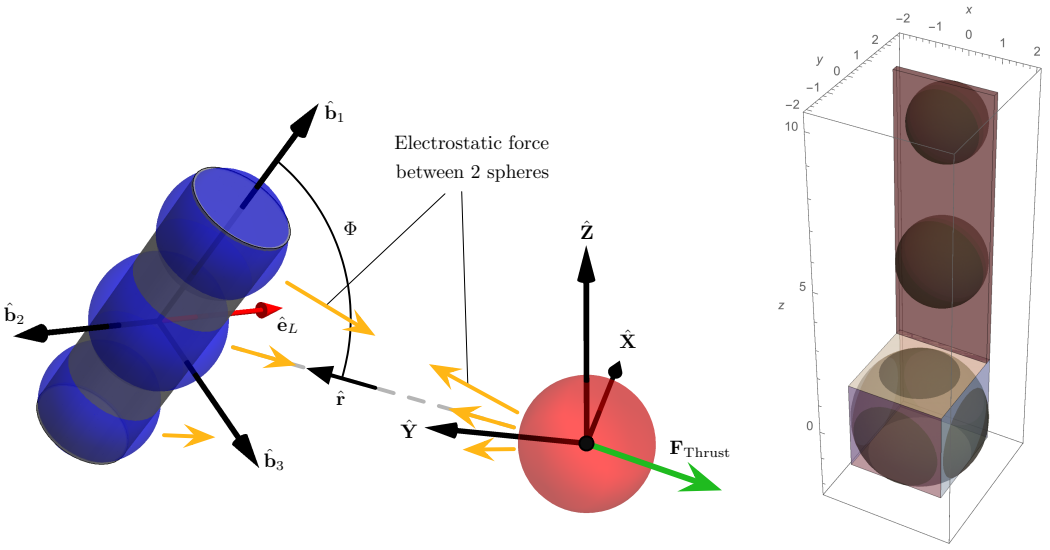


(a) Rocket body analog. (b) Box and panel geometry

**Figure 2. MSM sphere configurations for two target craft geometries.**

## RELATIVE POSITION IN ELECTROSTATIC MODELING

Modeling the electrostatic interaction faster than real time is required for on-orbit applications of electrostatic actuation. At present, finite element approaches to modeling this interaction produce single configuration results on the order of minutes. The Multi-Sphere Method (MSM) represents the spacecraft electrostatic charging model as a collection of spherical conductors carefully dispersed through the body reducing the computation time while retaining accuracy at the operational ranges considered.[36] The two considered models for this work are shown in Figure 2. The validated MSM approach allows faster than real time computation of electrostatic forces that account for relative position, charging, and attitude. The time-varying charges are computed from the prescribed electric potentials according to the self and mutual capacitance relationships in Eq. (1), where $k_c = 8.99 \times 10^9$ N·m$^2$/C$^2$ and $q_i$ is the charge of each sphere.[37,38]

$$\phi_i = k_c \frac{q_i}{R_i} + \sum_{j=1, j\neq i}^{m} k_c \frac{q_j}{r_{i,j}} \tag{1}$$

The term $R_i$ denotes the radius of the $i^{\text{th}}$ conducting sphere and $r_{i,j}$ denotes the vector between the $i^{\text{th}}$ and $j^{\text{th}}$ conducting spheres. These relations can be collected in matrix form for general application to all systems.

The force and torque experienced by the orbital target is computed by a summation of the force contributions between all spheres on the target and those on the servicer.

$$\boldsymbol{F}_2 = k_c q_1 \sum_{i=1}^{n} \frac{q_i}{r_i^3} \boldsymbol{r}_i \tag{2a}$$

$$\boldsymbol{L}_2 = k_c q_1 \sum_{i=1}^{n} \frac{q_i}{r_i^3} \boldsymbol{r}_{2,i} \times \boldsymbol{r}_i \tag{2b}$$

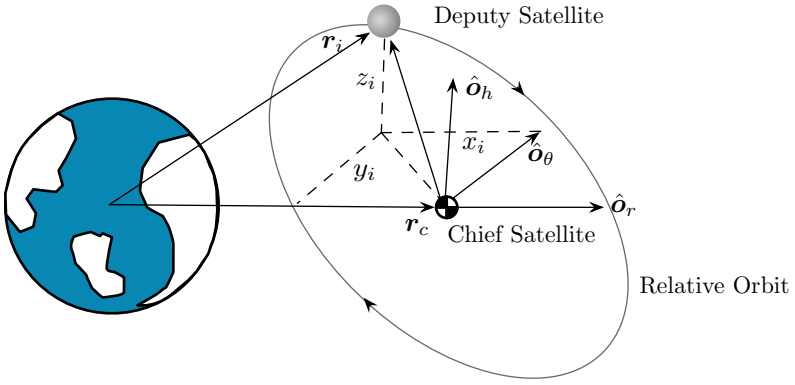


**Figure 3. Local vertical local horizontal rotating Hill frame for formation flying.[39]**

As seen in Eq. (2a) and Eq. (2b), the position between the consider spheres is included in the $\boldsymbol{r}$ term. Therefore, the relative position and attitude have strong influences on the force and torque experienced. Apart from the charge transfer process, the relative motion is a key element of the servicer control methodology. The final manuscript will present three sections on the formation flying guidance solutions, the navigation approaches that provide the necessary state information, and the control algorithms that deliver desired electrostatic interaction behavior.

## GUIDANCE OPTIMIZATION USING FORMATION FLYING APPROACHES

The servicer spacecraft is the only controlled craft for this study. As motivated by GEO applications, a circular reference orbit is utilized for the guidance of the servicer about the target craft. The relative motion of the considered ROEs are derived in the Hill frame defined in Figure 3. The Hill frame is defined by $\mathcal{H} = \{\hat{\boldsymbol{o}}_r, \hat{\boldsymbol{o}}_\theta, \hat{\boldsymbol{o}}_h\}$ where $\hat{\boldsymbol{o}}_r$ is aligned with the reference craft orbit radius, $\hat{\boldsymbol{o}}_h$ is aligned with the reference craft orbit angular momentum, and $\hat{\boldsymbol{o}}_\theta$ completes the orthonormal reference frame. The deputy spacecraft motion is described relative to a chief reference craft. Differencing the deputy spacecraft and the servider spacecraft positions provides the relative position vector $\boldsymbol{\rho} = (x, y, z)$ between the two craft. The relative position for this work is a represented in the Cartesian Hill frame in Figure 3. The recently developed Linearized Relative Orbit Elements (LROEs) provides a methods for optimizing reference trajectories, estimating the relative state, and controlling the servicer relative position.[33–35] The LROE state is extracted from the well known Clohessy-Wiltshire (CW) equations.[40]

$$x(t) = A_1 \cos(nt) - A_2 \sin(nt) + x_{\text{off}} \tag{3a}$$

$$y(t) = -2A_1 \sin(nt) - 2A_2 \cos(nt) - \frac{3}{2} nt x_{\text{off}} + y_{\text{off}} \tag{3b}$$

$$z(t) = B_1 \cos(nt) - B_2 \sin(nt) \tag{3c}$$

The constants in the CW equations become the otherwise time-invariant LROE state.

$$\boldsymbol{\alpha e} = \begin{bmatrix} A_1 & A_2 & x_{\text{off}} & y_{\text{off}} & B_1 & B_2 \end{bmatrix}^T \tag{4}$$

The LROEs defined in Eq. (4) are obtained from Cartesian Hill frame states through the inverse mapping in Eq. (5).

$$A_1 = -\frac{(3nx + 2\dot{y})\cos(nt) + \dot{x}\sin(nt)}{n} \tag{5a}$$

$$A_2 = \frac{(3nx + 2\dot{y})\sin(nt) - \dot{x}\cos(nt)}{n} \tag{5b}$$

$$x_{\text{off}} = 4x + \frac{2\dot{y}}{n} \tag{5c}$$

$$y_{\text{off}} = -\frac{2\dot{x}}{n} + y + (6nx + 3\dot{y})t \tag{5d}$$

$$B_1 = z\cos(nt) - \frac{\dot{z}\sin(nt)}{n} \tag{5e}$$

$$B_2 = -z\sin(nt) - \frac{\dot{z}\cos(nt)}{n} \tag{5f}$$

The analytic inverse allows Hill frame measurements to be easily mapped into LROE information without parameter singularities.[34]

**Variational Equations for Servicer Formation Control and Relative Navigation**

Gauss' variational equation is a classic result that shows how invariants of the unperturbed motion (i.e. inertial orbit elements) will vary in the presence of a perturbation accelerations.[41] This section derives the analogous variational equations for both the classical and new non-singular LROEs. The Lagrangian Bracket methodology evolves the invariants of motion present in a dynamical system's analytical solution to match the perturbed solution at the prescribed time. Given the inverse mappings provided in Eq. (5), the sensitivity matrices are computable. The LROE set $\boldsymbol{oe}$, otherwise invariant, evolves according to[39]

$$\dot{\boldsymbol{oe}} = [L]^{-1}\left[\frac{\partial \boldsymbol{r}}{\partial \boldsymbol{oe}}\right]^T \boldsymbol{a}_d \tag{6}$$

where $\boldsymbol{r}$ is the deputy position vector and $\boldsymbol{a}_d$ is the disturbance acceleration. The Lagrangian Bracket matrix $[L]$ is defined by

$$[L] = \frac{\partial \boldsymbol{s}}{\partial \boldsymbol{oe}}^T [J] \frac{\partial \boldsymbol{s}}{\partial \boldsymbol{oe}} \tag{7}$$

and $[J]$ is the symplectic matrix. A full description of the Lagrangian Bracket methodology is included in Chapter 12 of Reference 39. The equations of motion for the LROEs in Eq. (6) are simplified by defining the control matrix $[B]$ as

$$[B] = [L]^{-1}\left[\frac{\partial \boldsymbol{r}}{\partial \boldsymbol{oe}}\right]^T \tag{8}$$

allowing the LROE equations of motion to assume the following familiar dynamics form expressed in the local-vertical local-horizontal (LVLH) reference frame.

$$\dot{\boldsymbol{oe}} = [B]\boldsymbol{u} \tag{9}$$

This algebraic expression is similar to Gauss' variational equations for inertial orbit elements which is heavily used in perturbation and control studies. Applying this derivation approach to the invariants of the linearized relative motion will lead to the desired LROE variational equations. Furthermore, the form developed using Lagrangian Brackets is valid for both the rectilinear and curvilinear

LROE formulations.[34] The advantage of LROEs is evident by the availability of simple feedback relative orbit control with the specific implementation detailed in Eq. (10).[34]

$$\boldsymbol{u} = \boldsymbol{u}_r - ([B]^T[B])^{-1}[B]^T[K]\Delta\boldsymbol{oe} \tag{10}$$

**Demonstration of Formation Flying using LROEs**

Presented is a numerical analysis assumes Keplerian orbits with a equatorial circular LEO target with a semi-major axis of $a = 7550$ km. The simulated inertial state is composed of position and velocity vectors for both uncontrolled target spacecraft and controlled servicer spacecraft. The simulations are propagated for a duration of 10 servicer orbits to fully illustrate the near steady state behavior. The sample LROE reconfigurations considered transfer from a zero offset 2-1 ellipse to a lead-follower and back to the originating orbit. These cases demonstrate the breadth of the controller and target specific singularities or coupling effects that render the classical CW parameterization insufficient. Both transfers utilize full inertial non-linear simulations at an integration time step of 0.5 seconds.

Consider the first reconfiguration from the planar elliptic to leader-follower relative orbit. The initial and final LROEs for this reconfiguration are:

$$\boldsymbol{X}_0 = \begin{bmatrix} 20 & 0 & 0 & 0 & 0 & 0 \end{bmatrix}^T \text{ [m]} \qquad \boldsymbol{X}_r = \begin{bmatrix} 0 & 0 & 0 & 0 & 0 & 30 \end{bmatrix}^T \text{ [m]}$$

The second case considered is the return back to the initialized planar ellipse where the initial conditions and reference for the second case are the swapped values for the first case.

The gains in the positive definite matrix $[K]$ for the proposed control are selected via three considerations. First, expanding the $([B]^T[B])^{-1}[B]^T[K]$ product, some terms appear as $1/t$ or $1/t^2$. The gain terms preceding these higher order terms are set to zero for simplicity because the influence depletes as time moves towards infinity. This process eliminates most of the off-diagonal terms. It is therefore reasonable to assume a diagonal form for $[K]$.[34] Second, for a formation to be bounded or constrained to the desired drift the $x_{\text{off}}$ term must be as exact as possible. Thus, the gain for this term is set to an order of magnitude larger than the other errors in the LROE feedback. Third, the inverse LROE mapping in Eq. (5) is sensitive to large accelerations that switch the sign of the velocity too quickly. Inserting a mean motion multiplicative factor serves to spread the error over an entire orbit. Inspection of Eq. (5) as well as numerical simulations demonstrate that large shifts and significantly large gains cause an instantaneous shift in the LROEs obtained by the inverse mapping. Such rapid shift introduce error measures orders of magnitude larger leading to divergence. The feedback gain matrix $[K]$ is selected to be

$$[K] = n \cdot \text{diag}([1,\ 1,\ 30,\ 1,\ 1,\ 1]) \tag{11}$$

Remember that the gain on $x_{\text{off}}$ tracking errors is much larger than the other gains to ensure the bounded relative motion condition (i.e. $x_{\text{off}}$ = 0) is regained quickly.

The transfer between the initial and reference LROEs is dominantly achieved within 3 orbits. The Hill frame reconfiguration is shown in Figure 4 where the blue signifies the planar ellipse to lead-follower relative orbit reconfiguration with final point in blue. The return to the planar ellipse is shown in green with final point in green.

The modified LROEs time history provides additional insight into the reconfiguration. Shown in Figure 5 are the time histories of the two scaling terms $A_1$ and $A_2$ as well as the along track

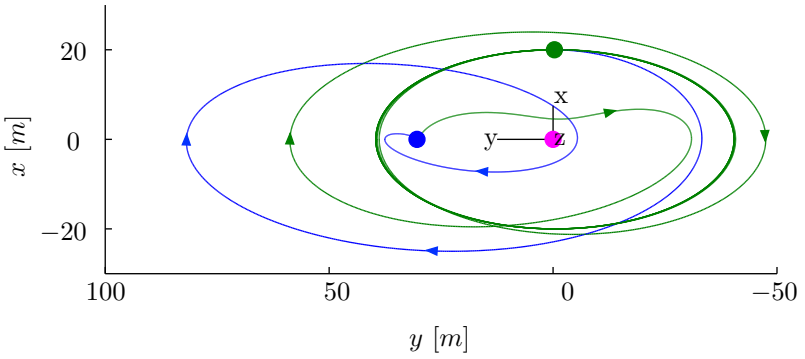


**Figure 4. Hill frame convergence from Planar Elliptic to Lead-Follower (—), and back to Planar Elliptic (—).**

and radial offsets with colors corresponding to the respective reconfigurations in the Hill frame; Figure 4.

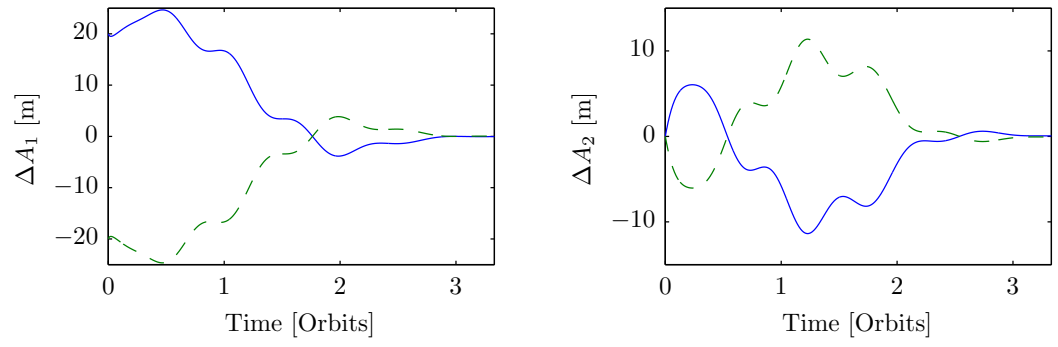


(a) $A_1$ Parameter Error

(b) $A_2$ Parameter Error

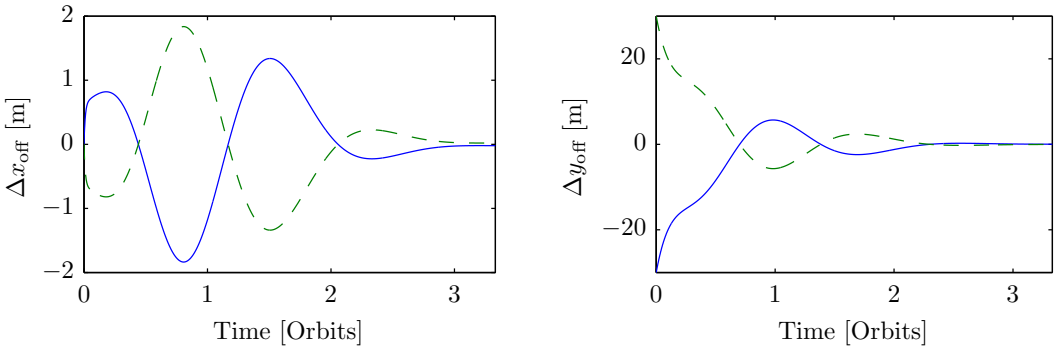


(c) $x_{\text{off}}$ Parameter Error

(d) $y_{\text{off}}$ Parameter Error

**Figure 5. LROE error for lead-follower to planar ellipse to lead-follower. Colors correspond to the relative motion in Figure 4.**

This methodology provides an elegant formulation of the dynamics that accounts for both control and disturbance perturbations. Furthermore, the use of the LROE state provides clear geometric insight into the influence and control of the relative position for electrostatic actuation applications. The final manuscript will demonstrate some of these insights for the considered target spacecraft geometries.

## CRITICAL PARAMETER ESTIMATION USING FORMATION FLYING

Of interest is the availability and quality of the relative state information necessary for computing relative forces and torques. The estimation of relative position using an LROE state was first demonstrated with an epoch state filter in the absence of perturbations.[35] An extension of this filter formulation introduces active electrostatic interaction and seeks to compute the charging properties of the two craft. The filters utilize a pose measurement camera for bearings and range measurements.

Simulating realistic camera noise, a set of two first order Gauss-Markov variables are propagated and added onto the bearing measurements. In general practice, Gaussian white noise is added to all measurement types. Therefore the measurements provided to the filter are computed by Eq. (12).

$$\mathrm{Az} = \mathrm{Az}_{\text{exact}} + \sigma_{\mathrm{Az}}^{GM} + w_{\mathrm{Az}} \tag{12a}$$

$$\mathrm{El} = \mathrm{El}_{\text{exact}} + \sigma_{\mathrm{El}}^{GM} + w_{\mathrm{El}} \tag{12b}$$

$$\rho = \rho_{\text{exact}} + w_{\rho} \tag{12c}$$

The inclusion of the Gauss-Markov process more accurately represents the expected performance of a visual navigation camera and the white noise provides the random noise source. The first-order Gauss-Markov random walk process is propagated using the form

$$\dot{\boldsymbol{\sigma}} = -B_{\text{GM}}\boldsymbol{\sigma} + W_k \tag{13}$$

where the $B$ matrix provides the time-constant-drive decay of the current variable value. The white noise process matrix $W_k$ is a randomly sampled value from a camera specific error covariance $W$. The $W$ matrix is the diagonal covariance of the camera white noise with elements $w_{\text{cam}}$. The camera considered in this study is a 5 mega-pixel, $n_{\text{p}} = 5 \times 10^6$, camera. The noise $w_p$ is assumed to be about 0.05 pixels for $3\sigma$ error. The camera is assumed to have a more narrow field of view with a half angle of $\alpha = 10^{\circ}$. This gives the radian noise magnitude of

$$w_{\text{cam}} = \frac{w_p}{n_{\text{p}}} * 2\alpha \tag{14}$$

### Illustration of Unperturbed Rectilinear LROE Relative Motion Estimation

The LROE extended Kalman filter formulation is implemented in a numerical simulation to demonstrate the feasibility and simplicity of estimating the LROE relative orbit given minimal sensor information.[35] The camera noise is defined in Eq. (14) and has a value of $1.56 \times 10^{-5}$ radians and a nominal range error of 2 centimeters at 200 meter range. To improve filter behavior, a measurement noise under-weighted to 5 times the true noise value as a preliminary filter tuning. The two satellites are inertially propagated with the full nonlinear two-body dynamics and are currently without perturbations. However, additional perturbations are easily included given the LROE dynamics provided by the Lagrangian Brackets.

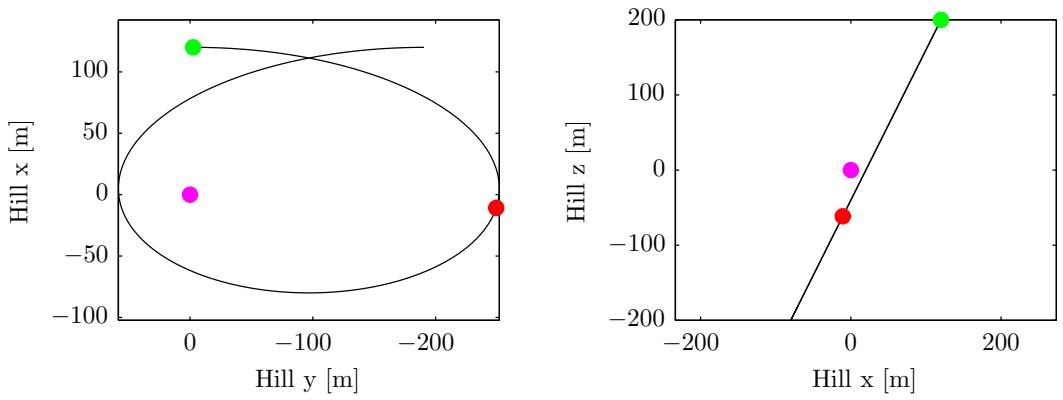


(a) Relative orbit, planar projection.

(b) Relative orbit, XZ projection.

**Figure 6. Hill frame relative orbit for the drifting relative ellipse example case. Start at o, finish at o about the chief.**

The chief spacecraft is initialized with a semi-major axis of 7500 kilometers and all other orbit elements as zero. The true relative orbit is initialized with $\boldsymbol{X}^{\text{true}}$ and the filter is given the initial conditions $\boldsymbol{X}^{\text{true}} + \Delta\boldsymbol{X}$. The LROE filter is applied to a drifting target satellite defined by the Cartesian initial conditions and filter state error as

$$\boldsymbol{X}^{\text{true}} = \begin{bmatrix} A_1 \\ A_2 \\ x_{\text{off}} \\ y_{\text{off}} \\ B_1 \\ B_2 \end{bmatrix} = \begin{bmatrix} 100 \\ 0 \\ 20 \\ \text{-}2.5 \\ 200 \\ 0 \end{bmatrix} \text{[m]} \qquad \Delta\boldsymbol{X} = \begin{bmatrix} 10 \\ \text{-}2 \\ 5 \\ \text{-}5 \\ \text{-}7 \\ 2 \end{bmatrix} \text{[m]} \tag{15}$$

The true drifting relative orbit over a simulated full orbit is shown in Cartesian Hill frame coordinates in Figure 6 with the filter cutoff at 0.3 orbits shown in red.

The results of two of the six states are presented here.[35] The presented LROE filtering pass only utilizes 0.3 relative orbits to converge to a reasonable answer. This speed of convergence from large initial condition errors is advantageous for space-to-space based observations because only fractions of an orbit are required to achieve the relative orbit estimate.

### Estimating Target Spacecraft Potential from Relative Motion

The estimation of the potential on both craft is critical to the control model for electrostatic actuation between spacecraft. The challenge of modeling the electrostatic potential on an instrumented craft has employed a variety of methods. Most notably, spacecraft potentials have been measured directly. The present approach demonstrates that the electrostatic perturbations produce sufficient alterations to the relative orbit to touchlessly obtain the charging behavior of the target craft. Recall from the LROE variational equations used in determining servicer thrust profiles for relative orbit reconfiguration may also capture the electrostatic interaction perturbations between the two craft. The electrostatic interaction is modeled using MSM described in Eq. (2a) and the perturbation accelerations are incorporated into the kinematic equations for the relative motion as described in Eq. (9).

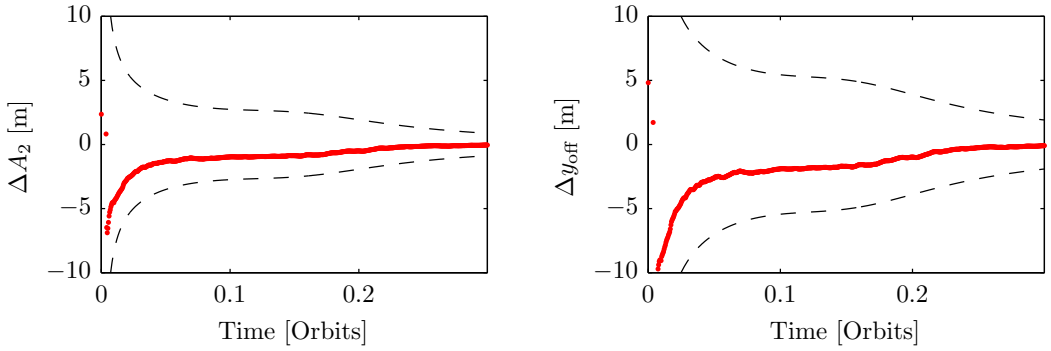


(a) $A_2$ state and $3\sigma$ variance.

(b) $y_{\text{off}}$ state and $3\sigma$ variance.

**Figure 7. LROE estimated state error and covariance envelopes highlighting full relative motion estimation for LROEs.**

An extended Kalman filter (EKF) is selected for the spacecraft electrostatic potential estimation simulation. The choice of a nonlinear filter enables the nominal LROE set to vary more dramatically and converge given poor, or absent, a priori. Furthermore, the EKF is a widely used filter and can be illustrative as a benchmark for the implementation of alternate estimation approaches. The filter state must include the desired is the spacecraft potential of the target craft. In addition, the relative motion of the two craft must also be included. Lastly, it is of interest to include the mass of the target as an uncertain parameter. The proposed filter state is the relative position of both the observer and target relative to the LVLH origin, the mass of the target, and the electrostatic potential of both craft.

$$\boldsymbol{X}_{\text{desired}} = \left[\boldsymbol{oe}_{\text{obs}},\ \boldsymbol{oe}_{\text{targ}},\ \phi_{\text{obs}},\ \phi_{\text{targ}}\right]^T \tag{16}$$

The inclusion of both an LROE state for each spacecraft is required because the electrostatic force will perturb both craft. However, only one of the two craft potentials is observable given relative separation observations. Examination of the LROE relative position in shows that the relative position in the LVLH frame may be described by differencing the Cartesian state which is equivalent to computing a Cartesian relative position using differential elements.[42]

$$\boldsymbol{\Delta S} = \boldsymbol{oe}_{\text{targ}} - \boldsymbol{oe}_{\text{obs}} \tag{17}$$

Therefore, the proposed filter estimates the differential relative position state and the target potential. The servicer/observer spacecraft may obtain estimates of its own potential through probes or ground-based observations.

$$\boldsymbol{X}_{\text{est}} = \left[\boldsymbol{\Delta S},\ \phi_{\text{targ}}\right]^T \tag{18}$$

Superb estimation of the LROE relative position is possible using short observational arcs.[35] The change in the relative position due to an electrostatic forces perturbation is much slower than the convergence of position-only estimation process. When the target craft potential is included in the rapid measurement updates used for relative position estimation, the extended Kalman filter tends to diverge. The filter divergence is a symptom of weak observability and computational precision. A simple solution for correcting this problem is to use longer propagation steps between measurement updates. However, the longer propagation gaps is less desirable for a servicer craft using the relative position estimate to perform station keeping. Therefore, a two-time-scale filter is proposed. Two-time-scale filters find application in estimation where elements of the dynamical system

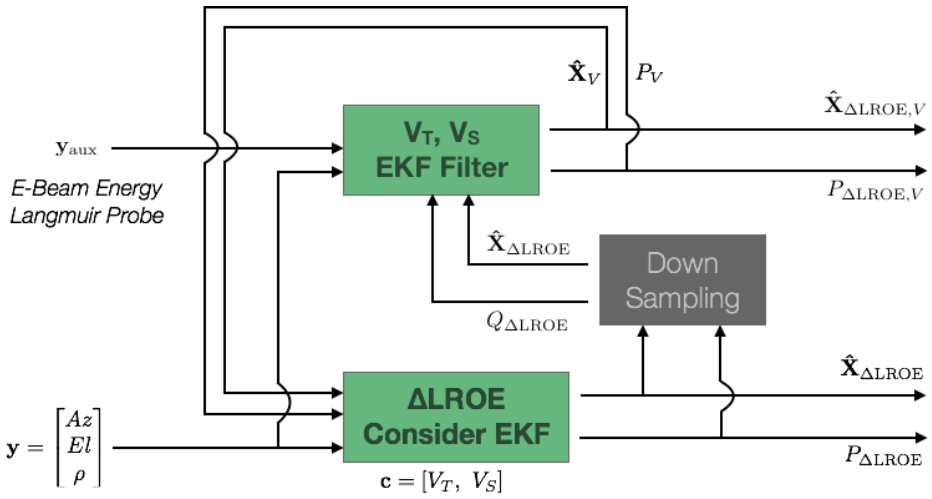


**Figure 8. Two-Time-Scale Filter Information Flow**

evolve on different time scales. An insightful example of two-time-scale filters is exhibited by the missile-intercept problem where the target vehicle may change course much faster than the smaller corrections to missile trajectory.[43] The two-time-scale estimation approach is directly applicable to the fast-evolving relative motion and the longer (or slower) observation of the target spacecraft electrostatic potential. Consider a nested set of estimation filters where the fast-estimate of the relative position is in part de-coupled from a longer propagation arc estimation of the proposed state in Eq. (18). The two-time-scale filter is shown in Figure 8.

The inner estimation filter that estimates the relative position, shown at the bottom of Figure 8, represents the fast-time estimation of the position. This estimate is achieved through a consider EKF and provides more frequent position information to the servicer spacecraft. The position estimation utilizes the current estimate of the target spacecraft potential with a consider covariance supplied by the outer filter. The outer estimation loop estimates the full state in Eq. (18) using the position from the inner loop to propagate the intermediate steps between updates.[43] This ensures that the outer filter computes an estimate on the best available relative position.

### Illustrative Electrostatic Potential and LROE Estimation Cases

The target spacecraft is initialized with a semi-major axis of 42160 kilometers and all other orbit elements as zero indicative of a GEO orbit. The true relative orbit is initialized with $\boldsymbol{X}^{\text{true}}$ and the filter is given the initial conditions $\boldsymbol{X}^{\text{true}} + \Delta\boldsymbol{X}$. The LROE filter is applied to a circumnavigating servicer satellite defined by the Cartesian initial conditions and filter state error as

$$\boldsymbol{X}^{\text{true}} = \begin{bmatrix} A_1 \\ A_2 \\ x_{\text{off}} \\ y_{\text{off}} \\ B_1 \\ B_2 \end{bmatrix} = \begin{bmatrix} 0 \\ \text{-}12.5 \\ 0 \\ 0 \\ 0 \\ \text{-}21.66 \end{bmatrix} \text{[m]} \qquad \Delta\boldsymbol{X} = \begin{bmatrix} 1 \\ 1 \\ 1 \\ 1 \\ 1 \\ 1 \end{bmatrix} \text{[m]} \tag{19}$$

The electrostatic potential is set to on the order of kilovolts to provide longer observation arcs.

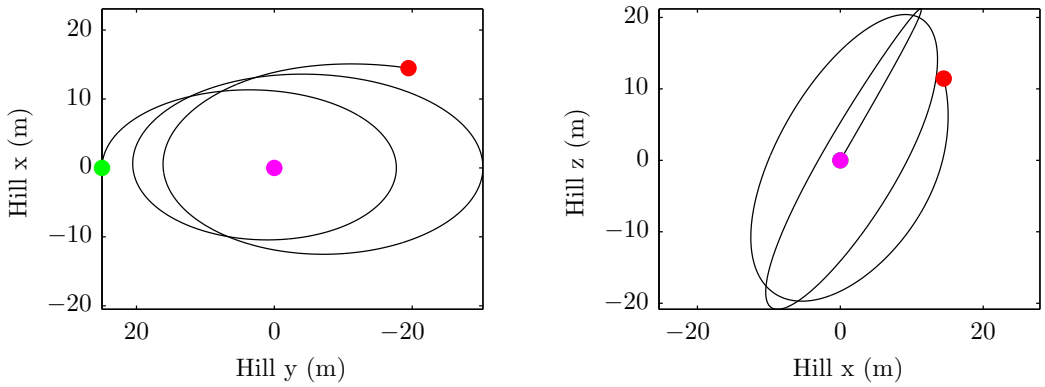


(a) Relative orbit, planar projection.

(b) Relative orbit, XZ projection.

**Figure 9. Hill frame relative orbit for the circularly projected example case. Start at o, finish at o about the target.**

The 20 kV magnitudes used for electrostatic detumble evolve much faster than an initialized two-time-scale filter is able to reasonably track. The estimation approach also introduces modeling error with the consider errors set to only kilovolt levels to provide longer duration measurement arcs without separating and consider errors on the order of what might be first achieved through auxiliary measurements and/or modeling.

$$\boldsymbol{C}_{\text{true}} = \left[\phi_{\text{obs}},\ \phi_{\text{targ}}\right]^T = [1900,\ -1700] \qquad \boldsymbol{c} = [10,\ -100] \tag{20}$$

The true drifting relative orbit over a simulated two orbit periods is shown in Cartesian Hill frame coordinates in Figure 9 with the filter cutoff shown in red. The presented Hill frame relative orbit is the basis for the more rapid relative position estimation and the less frequent updates to the target craft potential. The target craft electrostatic potential estimation is completed by the outer, slower time scale extended Kalman filter. The outer filter performs one measurement update for every 32 innner loop relative position updates.[42] Furthermore, the propagation of the combined LROE and electrostatic potential state utilizes the inner loop LROE estimate. The outer filter is delayed to allow the inner filter to converge first. The current realization of the filter waits for 10 estimation cycles, or 320 measurements, prior to performing the first update of the electrostatic potential. The start of the estimation and the convergence of the estimate is shown in Figure 10.

The final estimate of the target electrostatic potential differs by $\Delta\phi_{\text{tag}} \approx 36.4$ V down from the initialized -100 V error.[42] The present noise model and process noise, convergence of the covariance, and the bias in the servicer potential drive diminishing estimation returns following two orbit periods. However, the filter estimate of the target craft electrostatic potential is comparable to the error injected into the servicer craft potential. This filter demonstrates the feasibility of estimating electrostatic potential from relative motion and advantages of the two-time-scale estimation approach for electrostatic actuation applications.

## FORMATION FLYING METHODOLOGY FOR ELECTROSTATIC ACTUATION

Two target geometries are considered. The cylindrical target, representative of a booster upper stage, provides fundamental insights into electrostatic actuation and links to additional electrostatic

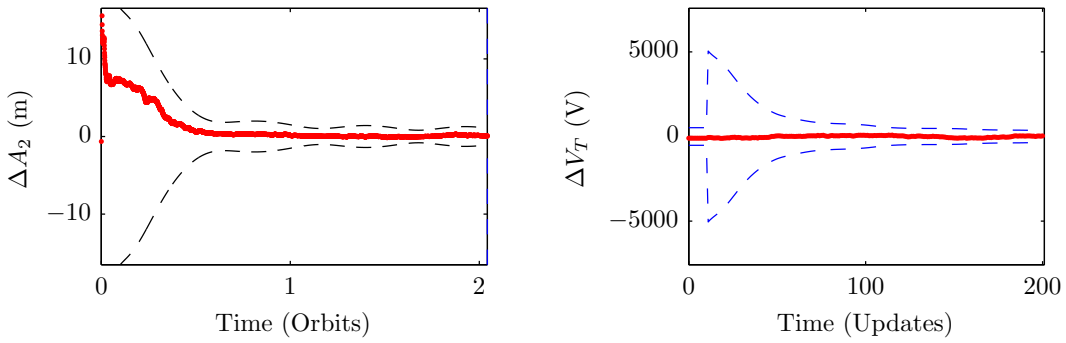


(a) $A_2$ state and $3\sigma$ variance.

(b) $V_T$ state and $3\sigma$ variance.

**Figure 10. LROE and target potential estimated state error and covariance envelopes indicative of full relative motion estimation while refining electrostatic potential.**

charging research. The more general box-and-panel target provides key geometry features representative of on-orbit satellite configurations.

Consider first the cylindrical target in Figure 2(a). The projection angle formulation sufficiently captures the detumble-specific attitude behavior for 3-dimensional tumble. Therefore, the projection angle is employed as a feedback control variable. Noting that the moment of inertia about the torque axis $\hat{\boldsymbol{e}}_L$ is always perpendicular to $\hat{\boldsymbol{b}}_1$, Euler's equations of tumbling motion are written in terms of $\mathcal{E}$-frame components to yield the following three scalar differential equations[44]

$$I_a \dot{\omega}_1 = 0 \tag{21a}$$

$$I_t \dot{\eta} - I_a \omega_1 \dot{\Phi} \sin\Phi = 0 \tag{21b}$$

$$I_t \left( \ddot{\Phi} \sin\Phi - \eta^2 \frac{\cos\Phi}{\sin^2\Phi} \right) + I_a \omega_1 \eta = L \tag{21c}$$

In Eq. (21), the angular velocity measures $\eta$ and $\dot{\Phi}$, as well as the proposed electrostatic control torque $\boldsymbol{L}$, are defined by

$$\eta \equiv -\omega_2(\hat{\boldsymbol{r}} \cdot \hat{\boldsymbol{b}}_2) - \omega_3(\hat{\boldsymbol{r}} \cdot \hat{\boldsymbol{b}}_3) \tag{22a}$$

$$\dot{\Phi} \sin\Phi = -\omega_2(\hat{\boldsymbol{r}} \cdot \hat{\boldsymbol{b}}_3) + \omega_3(\hat{\boldsymbol{r}} \cdot \hat{\boldsymbol{b}}_2) \tag{22b}$$

$$\boldsymbol{L} = -L\hat{\boldsymbol{e}}_L = -\gamma f(\phi)\, g(\Phi)\, \hat{\boldsymbol{e}}_L \tag{22c}$$

where the control torque $\boldsymbol{L}$ is summarized here.

Representing the equations of motion in the projection angle coordinate system $\mathcal{E}$ shows that the control only influences torques around the cylinder's transverse $\hat{\boldsymbol{e}}_L$ axis. Consistent with the assumption of an axi-symmetric geometry, there exists no control authority in the $\hat{\boldsymbol{b}}_1$ axis scalar equation and no cross coupling is present. Thus, $\omega_1$ is constant for all time. Revising the control formulation in Reference 31 leads to the new control law $f(\phi_1)$ for regulating the servicer craft potential, $\phi_1$:

$$f(\phi_1) = -\text{sgn}\left( \sum_{m=1}^{n} g_m(\Phi) \right) h(\alpha\dot{\Phi}) \tag{23}$$

where $\alpha > 0$ is a constant feedback gain and the function $h$ is chosen for stability such that:[31]

$$h(x)x > 0 \quad \text{if } x \neq 0 \tag{24}$$

Large tumble rates that tend toward infinity necessitate a limit on commanding a physical potential. The following $h$ function smoothly limits, or saturates, the control at a maximum achievable potential.[31]

$$h(\alpha\dot{\Phi}) = f(\phi_{\text{max}})\frac{\arctan(\alpha\dot{\Phi})}{\pi/2} \tag{25}$$

This control formulation is derived using the deep space assumption that the relative position is not changing. However, References 44 and 33 explain that the relative motion contribution to relative attitude change is sufficiently small to apply a deep space control formulation over most of the detumble mission. The benefits of formation flying while retaining the more simple deep space control formulation are shown in the following sections. The deep space control is also re-examined for non-axisymmetric targets.

**Lead-Follower Detumble Performance Improvement - Cylinder**

A lead-follower orbit as applied to the electrostatic detumble case consists of the servicer craft leading the target in the same orbit. The separation distance from center-to-center is 12.5 meters and can be described by a true anomaly difference or an LROE $y_{\text{off}} = 12.5$. The relative motion is regulated using the LROE feedback controller provided in a previous section. The deep-space detumble control design described in Eq. (23) is able to reduce the deep space angular momentum of a cylinder with an initial angular velocity magnitude of 2°/sec in about 10 days as shown in the top row of Figure 11.

Figure 11(a) clearly highlights the predictability of the electrostatic detumble in deep space provided by momentum analysis. However, shown in Figure 11(b), the angular velocity is reduced but not eliminated recalling that the symmetrical axis spin $\omega_1$ will not be removed. Inspection of the on-orbit case in Figure 11(d) demonstrates the convergence of the $\omega_2$ and $\omega_3$ terms with similar detumble time to the deep space case. The relative motion introduces greater momentum observability by the servicer leading to more effective momentum removal. As expected, the body frame angular velocities for the on orbit cases are reduced to nearly zero while the slender axis $\omega_1$ remains unaffected. The on-orbit projection angle, Figure 11(c), collapses to $90^\circ$ defined by the relationship of the relative motion and angular momentum vector while the deep-space steady-state projection angle is predicted by the phase-space relationship.

The circumnavigation of the servicer craft about the tumbling cylinder in a simple lead-follower configuration demonstrates a more complete detumble in the same amount of time. This is attributed to the systematic reconfiguration away from torque-free relative attitudes. Optimization of the relative orbit may further reduce detumble time and residual momentum.

**LROE Relative Orbit Optimization for Detumble Performance**

The angular momentum as seen in the relative frame provides key insights for relative orbit optimization. In the absence of perturbations, the inertially-fixed angular momentum vector $\boldsymbol{H}$ appears to cone in the rotating local-horizontal local-vertical, or Hill, frame in accordance with $H^{\mathcal{H}} = [\mathcal{H}\mathcal{N}]H^{\mathcal{N}}$ where $\mathcal{H}$ is the relative frame, and $\mathcal{N}$ is the inertial frame with coordinate system

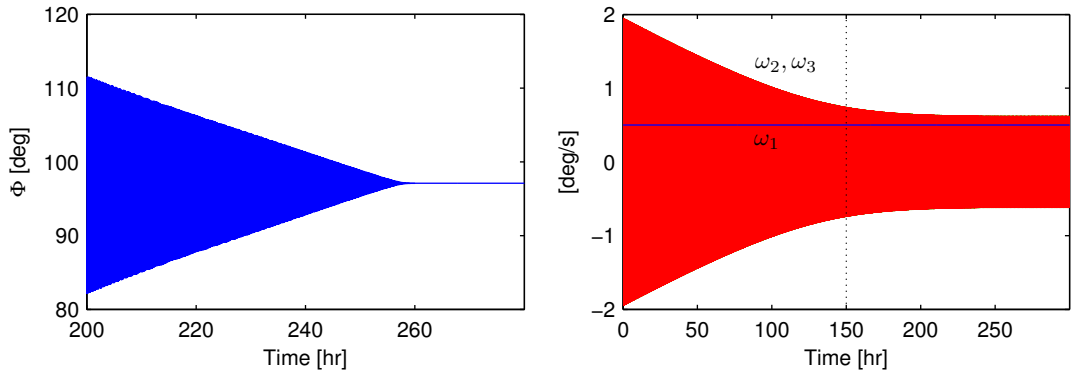


(a) Projection Angle, Deep Space

(b) Body Angular Velocities, Deep Space

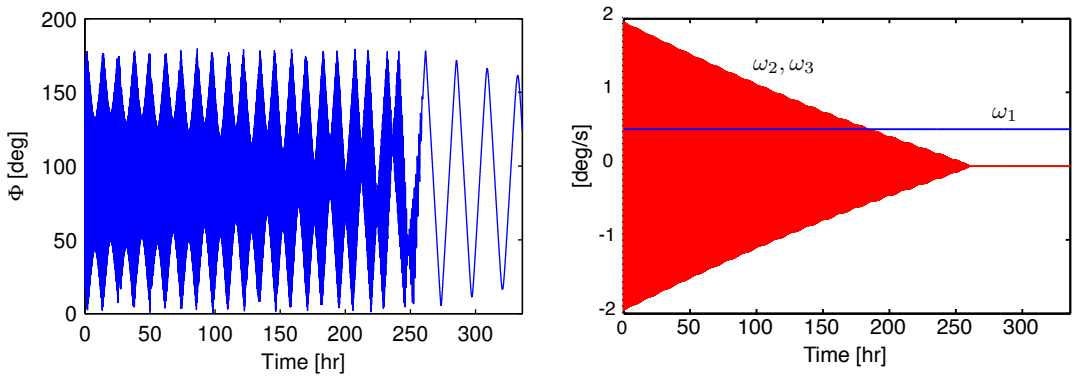


(c) Projection Angle, On Orbit

(d) Body Angular Velocities, On Orbit

**Figure 11. Numerical simulation with initial conditions: $\omega = [0.5, -1.374, \ 1.374]^\circ/$sec, $\Phi_0 = 30^\circ$ comparing both deep space (top row) and on orbit (bottom row).**

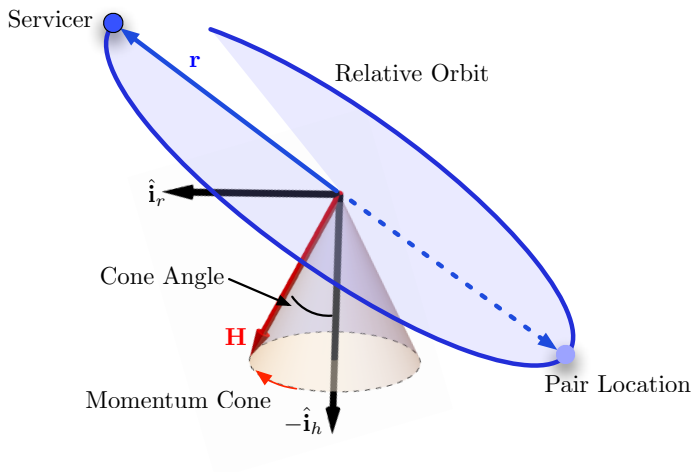


**Figure 12. Representation of the angular momentum coning present in the Hill frame.**

rotation matrix $[\mathcal{HN}]$. This is exemplified in Figure 12 where the target cylinder is the center of the Hill frame and the servicer position is controlled.

The relative orbit as seen in the Hill frame $\mathcal{H} = [\hat{\boldsymbol{\imath}}_r, \hat{\boldsymbol{\imath}}_\theta, \hat{\boldsymbol{\imath}}_h]$ is shown in Figure 12 as the blue swept relative ellipse. The inertially fixed angular momentum vector $\boldsymbol{H}$ precesses through a cone centered on the Hill frame orbit normal. The precession of this vector is leveraged to inform a relative orbit that enhances the detumble performance.

Proposed is an optimization cost function that minimizes both the separation distance and minimizes the off-perpendicular alignment of the relative position and momentum vector. First considered is a cost function that utilizes just the torque obtained for the particular relative position and attitudes about the angular momentum vector. However, this approach introduces local minima because the cost function relies on a sweep of attitudes and additional discretization assumptions. Therefore, a more general cost function that does not require instantaneous attitude information is explored to help reduce the number of local minima. The relative orbit elements are selected as the optimization state variables because these elements are directly sensed and controlled by the servicer spacecraft. Any optimization over the detumbling time and fuel usage requires multi-day GEO simulations at small time scales and thus large computational effort. However the detumbling time is directly proportional to the relative orbit configuration and inversely proportional to the separation distance. Thus, a cost function that maximizes the geometrical detumble torque opportunity and minimizes the separation distance achieves reductions in detumble time. The inclusion of relative position in the cost function allows the optimizer to trade significant improvements in geometry for separation distance.

$$J = \sum_{i=0}^{N} \left( -1000 \ln[|\boldsymbol{r}_i| - r^* + 1] - 10 \ln \left[ \left| \frac{\boldsymbol{r}_i \cdot \boldsymbol{H}_i}{\|\boldsymbol{r}_i\| \|\boldsymbol{H}_i\|} \right| + 1 \right] \right) \tag{26}$$

The cost in EQ. (26) is accumulated over a single discretized relative orbit with $N$ time segments. This approach utilizes 50 uniform time segments. The relative position and angular momentum are expressed in the Hill frame where $\boldsymbol{r}_i = \boldsymbol{r}(t_i)$ and $\boldsymbol{H}_i = \boldsymbol{H}(t_i)$ at time $t_i$. The minimum separation distance is prescribed by $r^*$. The relative weights are selected to achieve the same order of magnitude contribution for both separation distance and angle error. Both values are increased by an order of magnitude to help the convergence characteristics of the `fmincon` optimizer.

Only positive values of the LROE state are considered. This limits the relative orbit space to only the positive combinations, however it captures the full space in the cost function. The cosine cost, from the dot product, is symmetric about $\pi/2$ radians. Recall that the angular momentum traces a cone as viewed in the Hill frame over a single orbit. The cost function seeks a relative position vector that is perpendicular to the angular momentum vector. This is achieved by the absolute value of the dot product approaching zero. Consider a relative orbit plane with a normal parallel to the centerline of the angular momentum cone as shown in Figure 12. Should the servicer reside in either point separated by a relative orbit phase angle of $\pi$, then both points will have equivalent cost because both points provide equivalent cosine angle magnitudes relative to the instantaneous angular momentum vector. This allows the LROE state search to be reduced to a subset of all available LROE combinations where the symmetry can be later invoked to create pairs of optimized relative orbits.

**Table 1. Simulation parameters for cylinder detumble system.**

| Parameter | Value | Units | Description |
|---|---|---|---|
| $R_1$ | 2 | m | Servicer radius |
| $m_1$ | 500 | kg | Servicer mass |
| $m_2$ | 1000 | kg | Cylinder mass |
| $I_a$ | 125.0 | kg·m$^2$ | Axial inertia |
| $I_t$ | 812.5 | kg·m$^2$ | Transverse inertia |
| $\omega_0$ | 2 | deg/sec | Cylinder tumble |
| $\alpha$ | $5 \times 10^4$ | - | Control Gain |
| $\phi_{max}$ | 20 | kV | Max voltage |

**LROE Optimization of Servicer Relative Trajectory - Cylinder**

The simulation initializes the servicer spacecraft 12.5 meters away from a generally tumbling cylinder using the optimized output state. The numerical simulation includes the 6-DOF motion of the debris and 3-DOF translational motion of the servicer sphere. The closed-loop feedback control in (10) is used to maintain a fixed relative position between servicer and debris. A 4$^{\text{th}}$ order Runge-Kutta integration is employed with a time step of 0.01 seconds for 14 days. The servicer vehicle potential is controlled via (23) and the charging model in Reference,[45] while the electrostatic force is evaluated using the full MSM model in Eq. (2b).

The gain developed for the LROE controller is set to provide a bounding box of 1% of the relative separation distance. The gain is scaled by the mean motion of the chief orbit such that the relative motion leverages the natural dynamics of formation flying.

$$[K] = (n \cdot 10^5) \times \text{diag}([1,\ 1,\ 30,\ 1,\ 1,\ 1]) \tag{27}$$

The gain matrix utilized may not be optimal, however sufficient performance is obtained. Future studies will address the gain matrix and seek dynamical system leverage in precisely scaling the gain values. Using the `fmincon` optimization approach, the optimized LROE state and lead-follower state are set to

$$\begin{aligned} \boldsymbol{X} &= [A_1, A_2, x_{\text{off}}, y_{\text{off}}, B_1, B_2]\ [\text{m}] \\ \boldsymbol{X}_0^{\text{opt}} &= [0,\ 6.25,\ 0,\ 0,\ 0,\ 10.83]\ [\text{m}] \\ \boldsymbol{X}_0^{\text{lf}} &= [0,\ 0,\ 0,\ 12.5,\ 0,\ 0]\ [\text{m}] \end{aligned}$$

Utilizing the LROE control scheme over the 14 day simulation period, the optimized LROE orbit and the lead-follower orbit follow the paths shown in Figure 13. The LROE controller keeps the relative orbit close to the desired state through feedback control. The position error distance between the actual and reference trajectory never exceeds 20 centimeters. If desired, implementation of a more aggressive control would reduce the state error further.

Of interest is the reduction in angular momentum as seen by the Hill frame as shown in Figure 14.. Recall that the optimization approach leverages the revolution of the angular momentum in the Hill frame to design a relative trajectory. Inspection of Figure 14 reveals that the optimized ellipse delivers a more complete detumble in the radial and transverse directions where the lead-follower

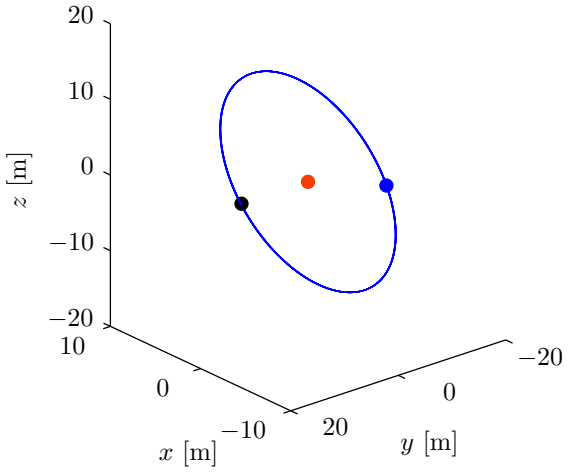


**Figure 13. The optimized state in blue and the lead-follower in black.**

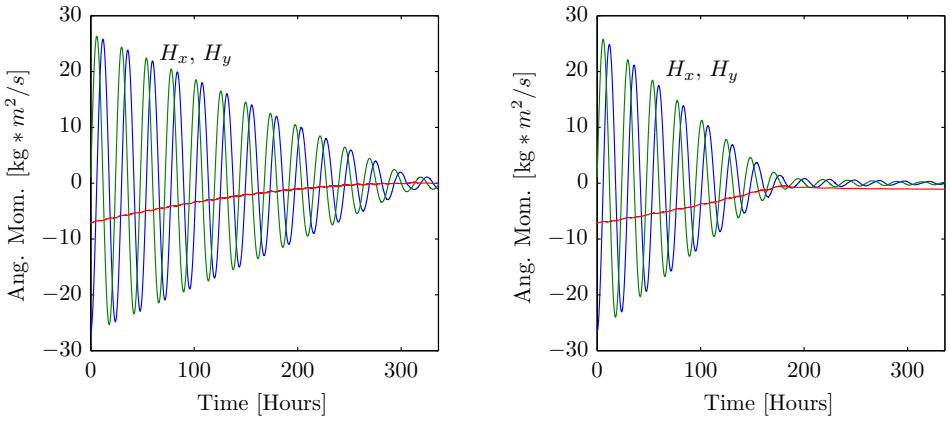


(a) Lead-follower configuration.

(b) Optimized LROE orbit.

**Figure 14. Hill frame momentum and detumble performance for a large cone angle.**

provides more complete reduction of the orbit-normal angular momentum. This is consistent with the relative position advantages where the lead-follower is most often perpendicular to the orbit normal where the optimized state provides a relative position that is more perpendicular to the orbit radial and along-track directions. This alignment is further seen in Figure 15 where the cross product between the relative position and angular momentum vector is subtracted from unity. Note that best detumble alignment occurs when the relative position vector is perpendicular to the angular momentum vector: a cross product of unity and thus a deviation of zero. The GEO orbit period of the relative orbit emerges in the daily cyclic drops in alignment benefit for both the lead-follower and the LROE configurations. However, it is quite evident that the LROE configuration consistently is better aligned for the removal of angular momentum. The cross product becomes more variable for the optimized state following the transition from primary to secondary detumble phases. Transition

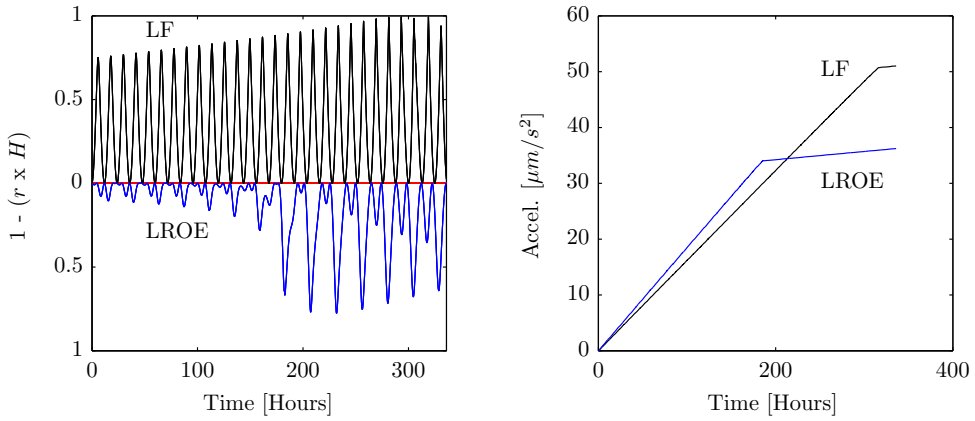


(a) Lead-follower and Optimized.

(b) Accumulated acceleration.

**Figure 15. Detumble geometry and orbit maintenance for a large cone angle.**

points, such as that following the primary detumble, suggests that the optimization approach could be re-applied to obtain a new optimized LROE state later reached by the LROE feedback controller.

The station-keeping acceleration for both the lead-follower and the optimized state is shown in Figure 15. The transition from primary to secondary detumble phases is clearly jointed for both LROE states which is attributed to the arctan control decrease for small angular velocities. The total acceleration is comparable between the two relative orbits. However, the variation in the relative orbit seen in Figure 13 suggests that the control gain should be more aggressive to reduce the variation in the state due to the electrostatic perturbations. A more aggressive controller may exaggerate the acceleration requirement differences between the two states. In addition, the control implemented is only a feedback control where the provided LROE form enables feed-forward capability.

### Expanding the Formation Flying Approach to More General Targets

The generic target detumble scheme employs an MSM distribution to compute the expected torque rather than an analytical approximation. The volume MSM distribution is most attractive for this application as it requires the fewest number of spheres to capture the electrostatic force and torque behavior.[46] The reduced number of spheres translates to reduced computational load on a flight software system. Consider the more generic target Lyapuov function in Eq. (28) where $\boldsymbol{\omega}$ is the body angular velocity vector and $I$ is the body-fixed inertia.

$$V = \frac{1}{2}\boldsymbol{\omega}^T I \boldsymbol{\omega} \tag{28}$$

Taking one time derivative of Eq. 28 and inserting Euler's rotational equations of motion, as is done in Eq. (21), produces the result in Eq. 29.

$$\dot{V} = \boldsymbol{\omega}^T \boldsymbol{L} \tag{29}$$

The simplicity of the Lyapunov derivative in Eq. (29) is made possible by neglecting the relative orbit motion thus assuming that the relative tumble is equal to body angular velocities. This is a

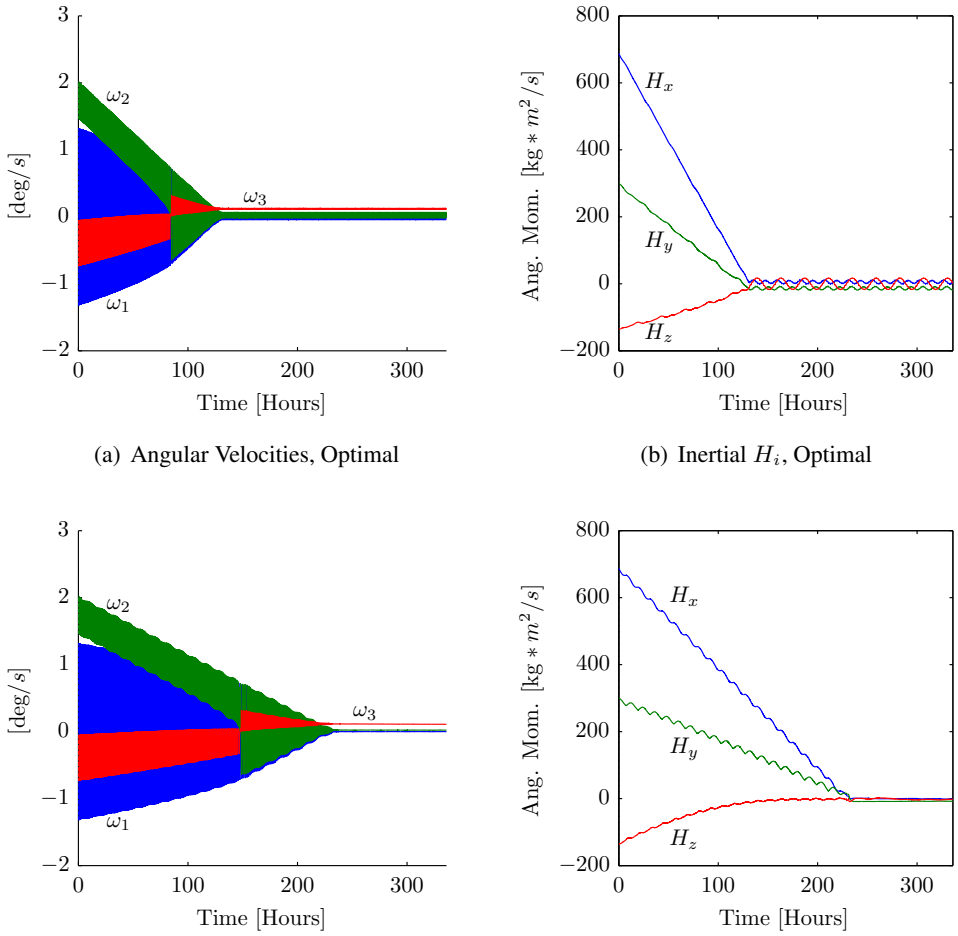


(a) Angular Velocities, Optimal

(b) Inertial $H_i$, Optimal

(c) Angular Velocities, Lead-Follower

(d) Inertial $H_i$, Lead-Follower

**Figure 16. Angular momentum and velocities with initial conditions: $\boldsymbol{\omega} = [0.9,\ 1.7,\ -0.6]^\circ$/sec, comparing optimized (top row) and lead-follower (bottom row).**

reasonable assumption for significant portions of the detumble mission as is seen for the on-orbit detumble of the cylindrical target. To achieve Lyapunov optimal control, the commanded servicer potential assumes the value[46]

$$\phi_{\text{cmd}} = C_\phi \times \{\text{sign}(\phi) : \boldsymbol{\omega}^T \boldsymbol{L}(\phi) \leq 0\} \quad \text{where} \quad C_\phi > 0 \tag{30}$$

The control law in Eq. (30) is Lyapunov optimal and guarantees, with perfect knowledge, that the servicer will detumble the target. Setting the coefficient $C_\phi$ to $\phi_{\text{max}}$ provides a bang-bang type control. The leading coefficient may be scaled based on the angular velocity to emulate the tangent saturation controller so long as the coefficient is always non-zero positive.

The box-and-panel target shown in Figure 2(b) is detumbled in Figure 16 using the generic control. The target is initialized in a flat momentum cone where the tumble about the body axes is given by $\boldsymbol{\omega} = [0.9,\ 1.7,\ -0.6]^\circ$/sec. Here, the optimized relative orbit is much more suited to removing angular momentum than a lead-follower.

## CONCLUSIONS

The guidance, navigation, and control necessary for on-orbit electrostatic detumble of both cylindrical and generic shapes are presented. The Linearized Relative Orbit Elements (LROEs) provide a convenient form for describing, estimating, and regulating the relative orbit. The application of LROEs further allows for estimation of the target craft potential as required by the detumble control formulations. The LROEs are last applied to optimization of the relative trajectory to reduce on-orbit detumble time and provide more complete angular momentum reduction. The presented work provides an overview of the electrostatic modeling, the control formulations, and the formation flying benefits for implementing electrostatic detumble on many orbiting targets.

## ACKNOWLEDGEMENTS

The authors would like to thank the NASA Space Technology Research Fellowship (NSTRF) program, grant number NNX14AL62H, for support of this research.

## REFERENCES

[1] P. Chrystal, D. McKnight, P. L. Meredith, J. Schmidt, M. Fok, and C. Wetton, "Space Debris: On Collision Course for Insurers?," tech. rep., Swiss Reinsurance Company Ltd, Zürich, Switzerland, March 2011.

[2] P. V. Anderson and H. Schaub, "Methodology for Characterizing High-Risk Orbital Debris in the Geosynchronous Orbit Regime," *AAS/AIAA Space Flight Mechanics Meeting*, Williamsburg, VA, Jan. 11–15 2015. Paper AAS 15-204.

[3] P. Couzin, F. Teti, and R. Rembala, "Active Removal of Large Debris: System approach of deorbiting concepts and Technological issues," *6th European Conference on Space Debris*, Darmstadt, Germany, April 22–25 2013. Paper No. 6a.P-17.

[4] Y. S. Karavaev, R. M. Kopyatkevich, M. N. Mishina, G. S. Mishin, P. G. Papushev, and P. N. Shaburov, "The Dynamic Properties of Rotation and Optical Characteristics of Space Debris at Geostationary Orbit," *Advances in the Astronautical Sciences*, Vol. 119, 2004, pp. 1457–1466. Paper No. AAS-04-192.

[5] A. A. Albuja, D. J. Scheeres, and J. W. McMahon, "Evolution of angular velocity for defunct satellites as a result of YORP: An initial study," *Advances in Space Research*, Vol. 56, July 2015, pp. 237–251, http://dx.doi.org/10.1016/j.asr.2015.04.013.

[6] J. Reed, J. Busquets, and C. White, "Grappling System for Capturing Heavy Space Debris," *2nd European Workshop on Active Debris Removal*, Paris, France, 2012. Paper 4.2.

[7] J. Starke, B. Bischof, W. H. Foth, and H. J. Guenther, "ROGER, a Potential Orbital Space Debris Removal System," *NASA/DARPA International Conference on Orbital Debris Removal*, Chantilly VA, December 8-10 2009.

[8] A. Caubet and J. D. Biggs, "Design of an Attitude Stabilization Electromagnetic Module for Detumbling Uncooperative Targets," *Aerospace Conference, 2014 IEEE*, Big Sky, MT, March 1-8 2014.

[9] N. Praly, M. Hillion, C. Bonnal, J. Laurent-Varin, and N. Petit, "Study on the eddy current damping of the spin dynamics of space debris from the Ariane launcher upper stages," *Acta Astronautica*, Vol. 76, 2012, pp. 145–153.

[10] N. O. Gómez and S. J. Walker, "Eddy currents applied to de-tumbling of space debris: Analysis and validation of approximate proposed methods," *Acta Astronautica*, Vol. 114, Sept. - Oct. 2015, pp. 34–53, 10.1016/j.actaastro.2015.04.012.

[11] N. O. Gómez and S. J. Walker, "Guidance, Navigation, and Control for the Eddy Brake Method," *Journal of Guidance, Control and Dynamics*, Vol. 0, No. 0, 2016, 10.2514/1.G002081.

[12] C. Bombardelli and J. Pelaez, "Ion Beam Shepherd for Contactless Space Debris Removal," *AIAA Journal of Guidance, Control, and Dynamics*, Vol. 34, May–June 2011, pp. 916–920, 10.2514/1.51832.

[13] S. Kitamura, Y. Hayakawa, K. Nitta, S. Kawamoto, and Y. Ohkawa, "A Reorbiter for Large Geo Debris Objects Using Ion Beam Irradiation," *63rd International Astronautical Congress*, Naples, Italy, 2012. Paper No. IAC-12-A6.7.10.

[14] C. Bombardelli, H. Urrutxua, M. Merino, E. Ahedo, J. Pelaez, and J. Olympio, "Dynamics of Ion-Beam Propelled Space Debris," *International Symposium on Space Flight Dynamics*, Sao Jose dos Campos, Brasil, Feb. 28 – March 4, 2011 2011.

[15] J. H. Cover, W. Knauer, and H. A. Maurer, "Lightweight Reflecting Structures Utilizing Electrostatic Inflation," US Patent 3,546,706, October 1966.

[16] L. A. Stiles, H. Schaub, K. K. Maute, and D. F. Moorer, "Electrostatically inflated gossamer space structure voltage requirements due to orbital perturbations," *Acta Astronautica*, Vol. 84, Mar.–Apr. 2013, pp. 109–121, 10.1016/j.actaastro.2012.11.007.

[17] M. A. Peck, "Prospects and Challenges for Lorentz-Augmented Orbits," *AIAA Guidance, Navigation and Control Conference*, San Francisco, CA, August 15–18 2005. Paper No. AIAA 2005-5995.

[18] B. Streetman and M. A. Peck, "New Synchronous Orbits Using the Geomagentic Lorentz Force," *AIAA Journal of Guidance, Control, and Dynamics*, Vol. 30, Nov.–Dec. 2007, pp. 1677–1690.

[19] L. B. King, G. G. Parker, S. Deshmukh, and J.-H. Chong, "Spacecraft Formation-Flying using Inter-Vehicle Coulomb Forces," tech. rep., NASA/NIAC, January 2002. `http://www.niac.usra.edu`.

[20] J. Berryman and H. Schaub, "Analytical Charge Analysis for 2- and 3-Craft Coulomb Formations," *AIAA Journal of Guidance, Control, and Dynamics*, Vol. 30, Nov.–Dec. 2007, pp. 1701–1710.

[21] C. R. Seubert, S. Panosian, and H. Schaub, "Analysis of a Tethered Coulomb Structure Applied to Close Proximity Situational Awareness," *AIAA Journal of Spacecraft and Rockets*, Vol. 49, Nov. – Dec. 2012, pp. 1183–1193.

[22] S. Wang and H. Schaub, "Nonlinear Charge Control for a Collinear Fixed Shape Three-Craft Equilibrium," *AIAA Journal of Guidance, Control, and Dynamics*, Vol. 34, Mar.–Apr. 2011, pp. 359–366, 10.2514/1.52117.

[23] E. Hogan and H. Schaub, "Relative Motion Control for Two-Spacecraft Electrostatic Orbit Corrections," *AIAA Journal of Guidance, Control, and Dynamics*, Vol. 36, Jan. – Feb. 2013, pp. 240–249.

[24] E. Hogan and H. Schaub, "Space Debris Reorbiting Using Electrostatic Actuation," *AAS Guidance and Control Conference*, Breckenridge, CO, Feb. 3–8 2012. Paper AAS 12–016.

[25] U. Yamamoto and H. Yamakawa, "Two-Craft Coulomb-Force Formation Dynamics and Stability Analysis with Debye Length Characteristics," *AIAA/AAS Astrodynamics Specialist Conference and Exhibit*, Honolulu, Hawaii, Aug. 18–21 2008. Paper No. AIAA 2008-7361.

[26] M. A. Peck, B. Streetman, C. M. Saaj, and V. Lappas, "Spacecraft Formation Flying using Lorentz Forces," *Journal of British Interplanetary Society*, Vol. 60, July 2007, pp. 263–267.

[27] H. Yamakawa, M. Bando, K. Yano, and S. Tsujii, "Spacecraft Relative Dynamics under the Influence of Geomagnetic Lorentz Force," *AIAA Guidance, Navigation and Control Conference*, Toronto, Canada, Aug. 2–5 2010. Paper No. AIAA 2010-8128.

[28] H. Schaub and D. F. Moorer, "Geosynchronous Large Debris Reorbiter: Challenges and Prospects," *AAS Kyle T. Alfriend Astrodynamics Symposium*, Monterey, CA, May 17–19 2010. Paper No. AAS 10-311.

[29] D. F. Moorer and H. Schaub, "Hybrid Electrostatic Space Tug," US Patent 0036951-A1, Feb. 17 2011.

[30] D. F. Moorer and H. Schaub, "Electrostatic Spacecraft Reorbiter," US Patent 8,205,838 B2, Feb. 17 2011.

[31] H. Schaub and D. Stevenson, "Prospects Of Relative Attitude Control Using Coulomb Actuation," *Jer-Nan Juang Astrodynamics Symposium*, College Station, TX, June 25–26 2012. Paper AAS 12–607.

[32] T. Bennett and H. Schaub, "Touchless Electrostatic Detumbling while Tugging Large Axi-Symmetric GEO Debris," *25th AAS/AIAA Spaceflight Mechanics Meeting*, Williamsburg, Virginia, Jan. 11–15 2015. Paper AAS 15-383.

[33] T. Bennett and H. Schaub, "Capitalizing On Relative Motion In Electrostatic Detumbling Of Axi-Symmetric Geo Objects," *6th International Conference on Astrodynamics Tools and Techniques (ICATT)*, Darmstadt, Germany, March 14–17 2016.

[34] T. Bennett and H. Schaub, "Continuous-Time Modeling and Control Using Nonsingular Linearized Relative-Orbit Elements," *Journal of Guidance, Control, and Dynamics*, 2016/10/24 2016, pp. 1–10, 10.2514/1.G000366.

[35] T. Bennett and H. Schaub, "Relative Motion Estimation Using Rectilinear and Curvilinear Linearized Relative Orbit Elements," *AAS/AIAA Spaceflight Mechanics Meeting*, Napa Valley, California, Feb. 14–18 2016. Paper No. AAS-16-336.

[36] D. Stevenson and H. Schaub, "Multi-Sphere Method for Modeling Electrostatic Forces and Torques," *Advances in Space Research*, Vol. 51, Jan. 2013, pp. 10–20, 10.1016/j.asr.2012.08.014.

[37] W. R. Smythe, *Static and Dynamic Electricity*. McGraw–Hill, 3rd ed., 1968.

[38] J. Sliško and R. A. Brito-Orta, "On approximate formulas for the electrostatic force between two conducting spheres," *American Journal of Physics*, Vol. 66, No. 4, 1998, pp. 352–355.

[39] H. Schaub and J. L. Junkins, *Analytical Mechanics of Space Systems*. Reston, VA: AIAA Education Series, 2nd ed., October 2009.

[40] W. H. Clohessy and R. S. Wiltshire, "Terminal Guidance System for Satellite Rendezvous," *Journal of the Aerospace Sciences*, Vol. 27, Sept. 1960, pp. 653–658.

[41] R. H. Battin, *An Introduction to the Mathematics and Methods of Astrodynamics*. New York: AIAA Education Series, 1987.

[42] T. Bennett and H. Schaub, "Electrostatically Charged Spacecraft Formation Estimation Using Linearized Relative Orbit Elements," *AAS Spaceflight Mechanics Meeting*, San Antonio, TX, Feb. 5–9 2017. Paper AAS 17–483.

[43] S. A. R. Hepnar and H. P. Geering, "Adaptive Two-Time-Scale Tracking Filter for Target Acceleration Estimation," *Journal of Guidance*, Vol. 14, No. 3, 1991, pp. 581–588.

[44] T. Bennett, D. Stevenson, E. Hogan, L. McManus, and H. Schaub, "Prospects and Challenges of Touchless Debris Despinning Using Electrostatics," *Advances in Space Research*, Vol. 56, Aug. 2015, pp. 557–568, 10.1016/j.asr.2015.03.037.

[45] E. Hogan and H. Schaub, "Space Weather Influence on Relative Motion Control using the Touchless Electrostatic Tractor," *Journal of Astronautical Sciences*, Vol. 63, No. 3, 2016, pp. 237–262, 10.1007/s40295-016-0090-4.

[46] T. Bennett and H. Schaub, "Touchless Electrostatic Detumble Of A Representative Box-And-Panel Spacecraft Configuration," *European Conference on Space Debris*, ESOC, Darmstadt, Germany,, April, 18–21 2017.